

Identifying optical signatures of momentum-dark excitons in transition metal dichalcogenide monolayers

Jessica Lindlau¹, Cedric Robert², Victor Funk¹, Jonathan Förste¹, Michael Förg¹, Léo Colombier¹, Andre Neumann¹, Emmanuel Courtade², Shivangi Shree², Marco Manca², Takashi Taniguchi³, Kenji Watanabe³, Mikhail M. Glazov⁴, Xavier Marie², Bernhard Urbaszek², and Alexander Högele¹

¹Fakultät für Physik, Munich Quantum Center, and Center for NanoScience (CeNS),

Ludwig-Maximilians-Universität München, Geschwister-Scholl-Platz 1, 80539 München, Germany

²Université de Toulouse, INSA-CNRS-UPS, LPCNO, 135 Ave. de Rangueil, 31077 Toulouse, France

³National Institute for Materials Science, Tsukuba, Ibaraki 305-0044, Japan and

⁴Ioffe Institute, 26 Polytechnicheskaya, 194021 St. Petersburg, Russia

(Dated: October 26, 2017)

Transition metal dichalcogenide (TMD) monolayers (MLs) exhibit rich photoluminescence spectra associated with interband optical transitions of direct-gap semiconductors. Upon absorption of photons, direct excitons with zero center-of-mass momentum are formed by photo-excited electrons in the conduction band and the respective unoccupied states in the valence band of the same valley. Different spin configurations of such momentum-direct excitons as well as their charged counterparts provide a powerful platform for spin-valley and microcavity physics in two-dimensional materials. The corresponding spectral signatures, however, are insufficient to explain the main characteristic peaks observed in the photoluminescence spectra of ML TMDs on the basis of momentum-*direct* excitons alone. Here, we show that the notion of momentum-*indirect* excitons is important for the understanding of the versatile photoluminescence features. Taking into account phonon-assisted radiative recombination pathways for electrons and holes from dissimilar valleys, we interpret unidentified peaks in the emission spectra as acoustic and optical phonon sidebands of momentum-dark excitons. Our approach will facilitate the interpretation of optical, valley and spin phenomena in TMDs arising from bright and dark exciton manifolds.

Monolayer (ML) transition metal dichalcogenides (TMDs) are material representatives of a broader class of atomically thin direct-gap semiconductors [1, 2] pivotal for the realization of van der Waals heterostructures and devices with novel functionality [3–5]. They feature strong optical transitions promoted by excitons [6–9] and, paired with valley-selective excitation [10], manipulation [11–15] and detection [16–19] schemes, represent viable resources for opto-valleytronic applications [20–22]. While optical transitions of lowest-energy excitons in molybdenum-based MoSe₂, MoS₂ or MoTe₂ MLs is spin-allowed, the exciton ground state of ML tungsten dichalcogenides WSe₂ and WS₂ is spin-forbidden [23–30]. This striking difference stems from a reversed energetic ordering of spin-polarized conduction sub-bands in molybdenum and tungsten dichalcogenide MLs [31–35].

While early photoluminescence (PL) spectroscopy studies have established elementary signatures of bright excitons in neutral [6–8] and charged TMD MLs [36–38], the emission from spin-forbidden excitons has been identified only recently [23, 26–30]. The observations of lowest-lying momentum-bright yet spin-forbidden states in tungsten dichalcogenide MLs explain some of the differences between the rich structure in the PL spectra of tungsten-based MLs and the rather simple one- or two-peak PL of ML molybdenum dichalcogenides [39]. Some of the main PL peaks that can be more intense than the bright exciton, however, have escaped unambiguous assignment and are thus commonly attributed to defect-localized excitons. Moreover, unequivocal deconvolution of individual PL contributions from neutral and charged excitons has been compromised by the lack of control over the charge doping level in most samples and impeded further

by the conspiracy of similar energy scales of optical phonons [40, 41] and trion binding energies [19, 37, 42]. Here, we propose a unifying explanation for unidentified PL features in the spectra of TMD MLs by expanding the realm of momentum-direct excitons with their momentum-indirect counterparts. This analysis benefits from the greatly improved optical quality of TMD MLs encapsulated in hBN [29, 39, 43–45] in charge tunable structures.

Signatures of direct and indirect excitons in the emission spectra. First we describe our approach to decompose the optical spectra of ML TMDs involving momentum-dark exciton contributions. Subsequently, we demonstrate how this simple approach can be applied to reproduce the most prominent spectral features observed in PL. The basic understanding of the optical phenomena in TMD MLs derives from the single-particle band structure shown schematically in Fig. 1a. The conduction band (CB) and valence band (VB) feature spin-polarized sub-bands with energy splittings Δ_{SO} at K and K' points of the first Brillouin zone. The VB spin-orbit splitting of a few hundred of meV as estimated from first-principles calculations [31–33, 35] and determined experimentally [46, 47] is contrasted by a much smaller CB splitting Δ_{SO} on the order of a few to a few tens of meV [31–33, 35]. In addition to the K and K' valleys, the CB of TMD MLs exhibits local minima at six non-equivalent Q-pockets related pairwise by time-reversal symmetry [48, 49]. Depending on the specific material and the details of calculations, the Q-valley band-edges can be as far as $\Delta_{\text{KQ}} \simeq 160$ meV above the CB minimum as in MoSe₂, or in the range of ~ 0 –80 meV in tungsten-based MLs [35, 40, 50].

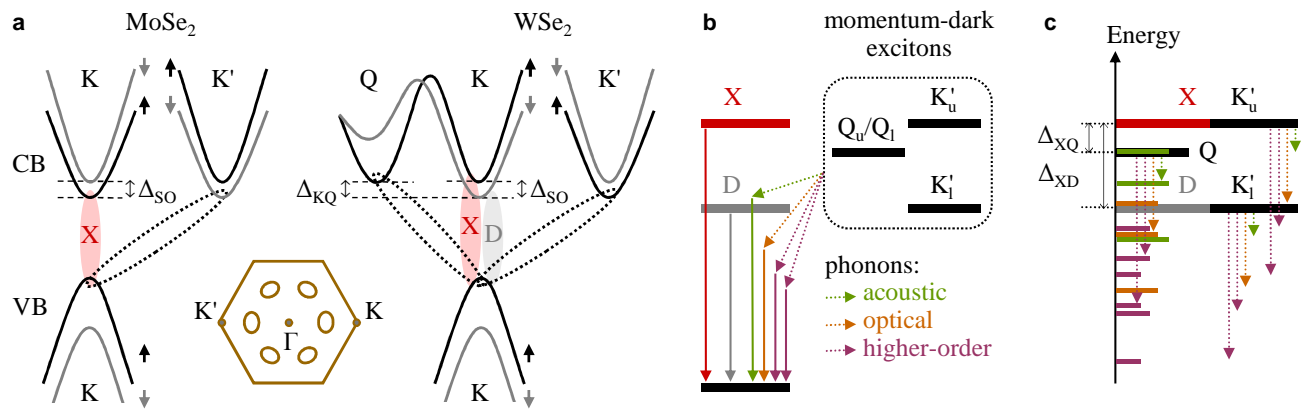


FIG. 1: **Basic concepts for the spectral decomposition of photoluminescence from monolayer transition metal dichalcogenides.** **a**, Schematic band structure in the first Brillouin zone (inset with high-symmetry points Γ , K and K' , and six inequivalent Q-pockets) of molybdenum (left) and tungsten (right) dichalcogenide monolayers. Conduction band (CB) and valence band (VB) with spin-up and spin-down electron sub-bands (shown in black and grey, respectively), spin-orbit splitting Δ_{SO} , and the energy separation Δ_{KQ} between the conduction band minima at K and Q. Momentum-direct spin-bright and spin-forbidden excitons (X and D, indicated by ellipses shaded in red and grey) are formed by electrons and unoccupied states in the K-valley. Momentum-dark excitons (dashed ellipses) with the empty state at K can be formed with electrons at Q or K' . **b** and **c**, With this realm of direct and phonon-assisted radiative processes, we construct a conceptual PL spectrum as the sum of the zero-phonon lines (ZPLs) of X and D excitons (red and grey bars) and the phonon side-bands of momentum-dark excitons (colored bars). The energy position of the latter (black bars) can be reconstructed from their respective phonon replicas (green and orange bars) by considering in-plane transverse acoustic (TA) and longitudinal acoustic (LA) phonons as well as in-plane $TO(E')$, $LO(E')$ and out-of-plane A_1 optical phonon modes, and sidebands resulting from higher order decay processes (purple bars) assisted by combinations of multiple phonons.

With this single-particle picture in mind we interpret the rich PL spectra of TMD MLs by including indirect transitions associated with electrons and holes in dissimilar valleys [51–55] as initially proposed by Dery and Song for combinations of electrons in K with empty VB states in K' in tungsten-based MLs [51]. To this end we construct excitons by forming an empty state in the upper valence sub-band at the K valley and the Coulomb-correlated electron at the K' or, alternatively, at one of the Q-points. Note that the hole state is formally associated with the time-reversal of the unoccupied state in the valence band [9]. Neglecting the upper sub-band at the Q-points due to sizable spin-orbit splittings of the order of 100 meV [35] and omitting electron-hole exchange for simplicity (energy scale of a few meV), we obtain the exciton spectrum shown schematically in Fig. 1b. Two zero-momentum configurations with both electron and hole at K correspond to the well studied spin-allowed and spin-forbidden exciton (X and D) [26–28, 30, 53, 56].

In addition to direct excitons, also excitons with finite center-of-mass momenta can be constructed from electrons in valleys other than the unoccupied state in K. They do not recombine directly via photon emission but require the assistance of acoustic or optical phonons. We label these momentum-dark excitons with capital letters denoting the electron valley with the subscript l (u) for spin-like (spin-unlike) configurations of the electron and hole spins (in electron spin notation). By neglecting electron-hole exchange we obtain two pairs of degenerate states with electrons and holes in K (D and K'_l as well as X and K'_u), and degenerate spin-like

and spin-unlike Q-excitons with electrons in six inequivalent Q-pockets. The energetic ordering in Fig. 1b corresponds to tungsten-based MLs. In the presence of time-reversal symmetry, all states have their counterparts with the unoccupied state at the K' -valley and reversed spin orientation.

As the manifold of momentum-dark excitons, shown encaged in Fig. 1b, has no dipolar radiative pathways due to momentum conservation constraints, the states do not appear directly in PL or reflection spectroscopy. However, in analogy to indirect band-gap bulk semiconductors such as silicon [57] or hexagonal boron nitride (hBN) [58], finite-momentum excitons can decay radiatively via simultaneous emission of phonons. Such decay channels, indicated schematically in Fig. 1b and c by colored arrows and enabled by acoustic and optical phonons as well as higher order combinations of multi-phonon processes, will give rise to phonon replicas of momentum-dark excitons in the PL emission. Once the energy positions of all states are determined from spectral decomposition, the splittings Δ_{XD} and Δ_{XQ} are obtained as indicated in Fig. 1c.

Analysis on monolayer MoSe₂ emission. First, we apply our analysis to ML MoSe₂ encapsulated in hBN with active doping control. The cryogenic PL spectrum shown in Fig. 2 features two bright PL peaks, commonly attributed to the emission from neutral and charged excitons. In high signal-to-noise differential reflectivity measurements in our gated structure, however, no trion signature was detected in addition to the solitary resonance of the neutral exciton (see Supplementary Information) in contrast to doped samples [59]. We

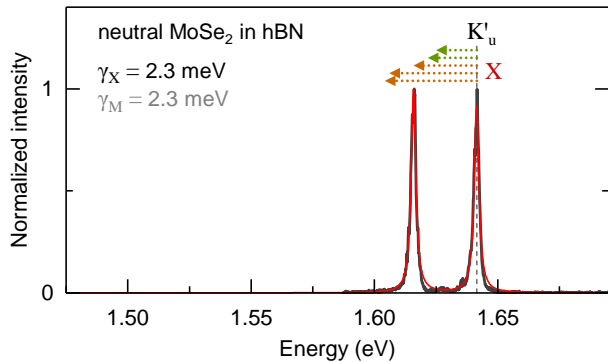


FIG. 2: **Spectral decomposition of cryogenic photoluminescence from monolayer MoSe₂.** Basic model fit (red solid line) with first-order phonon replicas of momentum-dark K'_u excitons resonant with the bright exciton state X in the absence of electron-hole exchange. The best-fit energy position indicated by the dashed line was obtained with γ_X as fit parameter and γ_M set identical to γ_X . The green and orange arrows indicate phonon sidebands of momentum-dark excitons associated with acoustic and optical phonons with respective energies taken from Ref. 40. Free (fixed) fit parameters are given in the legends in black (grey).

therefore argue that the intensive PL peak ~ 30 meV below X could also be interpreted as an optical phonon sideband of the momentum-dark exciton state K'_u that we set resonant with the bright exciton by neglecting electron-hole exchange. The respective acoustic sidebands would then contribute weak yet finite PL in between the two intensive peaks.

To obtain a model fit of the neutral ML MoSe₂ spectrum in the framework of this analysis shown by the red solid line in Fig. 2, we modeled the ZPLs of resonant momentum-bright and momentum-dark states X and K'_u by homogeneously broadened Lorentzians with the same full-width at half-maximum linewidth γ_X . Moreover, we restricted the phonon replicas of K'_u to first-order processes. By taking the corresponding phonon modes calculated in Ref. 40 (recapitulated in Table S1 of the Supplementary Information for convenience) with explicit phonon energies of 16.6, and 19.9 meV for the TA and LA acoustic phonons, and 35.5, 37.4, and 25.6 meV for TO(E'), LO(E') and A_1 optical phonons available for the scattering of the electron from the K' into the K-valley, we allowed the fitting procedure to determine the best-fit energy position (indicated by the dashed line) and linewidth $\gamma_X = 2.3$ meV for the ZPL of X and thus of K'_u .

Remarkably, the correspondence between the spectrum and the model fit in Fig. 2 was obtained with vanishing contributions from TO and LO phonons, and thus the lower-energy peak can be ascribed entirely to the A_1 optical sideband of K' . Our analysis of ML MoSe₂ PL from a more disordered sample (see Supplementary Information) indicates that both TO and LO phonons as well as higher-order phonon processes can be activated in the presence of disorder [60]. For phonon replicas to be as intense in emission as the bright exciton

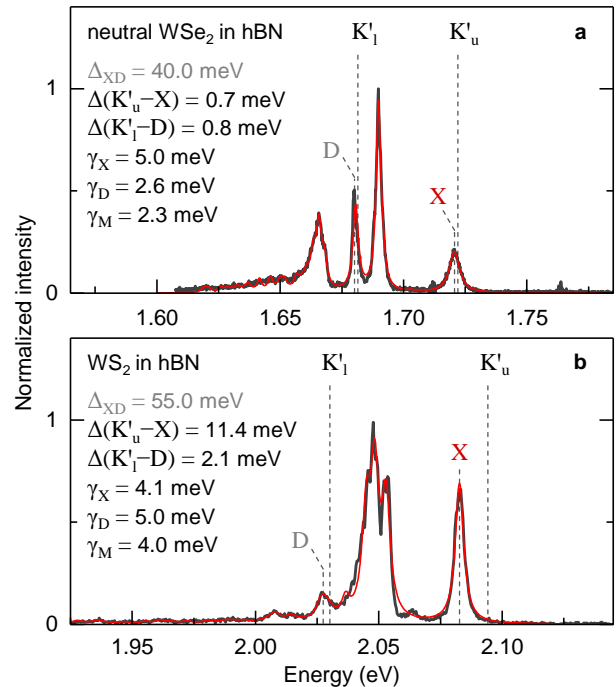


FIG. 3: **Spectral decomposition of cryogenic photoluminescence from monolayer WSe₂ and WS₂.** **a**, Refined model fit (red solid line) to the spectrum of neutral monolayer WSe₂ including momentum-dark state K'_1 resonant with D at a fixed bright-dark splitting $\Delta_{XD} = 40$ meV and all other parameters determined from the best fit. **b**, Same for monolayer WS₂ without active charge control. Free (fixed) fit parameters are given in the legends in black (grey).

emission in the PL of neutral ML MoSe₂, long-lived population of dark states without efficient decay channels must be present. Such population can be provided by the reservoir of momentum-dark K' excitons, or by momentum-dark Q states if the value of 28 meV [40] instead of the much higher prediction of 137 meV [35] is anticipated for the splitting Δ_{KQ} in ML MoSe₂.

Analysis of monolayer WSe₂ emission. The analysis of the simple MoSe₂ emission has served as an illustration of the possible involvement of phonon-assisted recombination of momentum-dark excitons. In the next step we apply our decomposition analysis to ML WSe₂ with a rich spectrum of unidentified peaks [19] as in Fig. 3a recorded on ML WSe₂ encapsulated in hBN and tuned to the point of charge neutrality [61]. It features narrow spectral lines characteristic of high-quality MLs with PL close to the homogeneous limit [30, 39, 44] and we assume a negligible contribution from trions, again based on the absence of a trion resonance in high signal-to-noise reflectivity. As discussed previously, the PL signatures of ML WSe₂ in Fig. 3a differ significantly from the PL of ML MoSe₂ in Fig. 2 because of the reversed ordering of spin-polarized sub-bands in tungsten and molybdenum based dichalcogenides. To model the PL spectrum of WSe₂, one has to include the spin-forbidden exciton state D red-shifted

by 40 meV from the ZPL of the bright state X in this specific sample [30, 61]. In order to obtain the best model fit shown as the red solid line in Fig. 3a, we allowed not only the phonon energies to vary around the values given for ML WSe₂ in Ref. 40 but also the energies and linewidths of the Lorentzian ZPLs of D, K'₁, K'_u, and X states. Assuming similar timescales for phonon-assisted decay and transform limited broadening of momentum-dark states, a joint linewidth γ_M was used for both states.

The best-fit model spectrum of Fig. 3a with up to third-order processes was obtained with $\gamma_X = 5.0$ meV and comparable linewidths of ~ 2.5 meV for both spin-forbidden and momentum-dark states at the respective energy positions of the ZPLs indicated by the dashed lines. The overall correspondence between the measured spectrum and the model is again compelling. It interprets the bright-most peak in between the bright and dark exciton ZPLs as composed of optical phonon replicas of the momentum-dark state K'_u, and the peak below D as acoustic sidebands of K'₁. We stress again that we do not attribute here the peak 32 meV below the bright exciton to trion emission for two reasons: First, the gated sample shows only one solitary resonance of the neutral exciton without additional trion features in differential reflectivity. Second, this sample tuned into the *n*-type regime exhibits a pronounced fine structure splitting both in PL and reflectivity as a hallmark of negative trions [61]. Without the ambiguity of unintentional doping, the electron-hole exchange splittings $\Delta(K'_u - X)$ and $\Delta(K'_1 - D)$ are of the order of a few meV.

Analysis of monolayer WS₂ emission. The analogous spectral decomposition was also carried out for ML WS₂ sandwiched in hBN without means of field-effect charge control. The best fit to the PL spectrum of Fig. 3b was obtained according to the refined fitting procedure used for ML WSe₂ in Fig. 3a with a fixed bright-dark splitting of 55 meV derived from experiment [30] and similar values for the linewidths of momentum-bright and dark excitons in the range of 4–5 meV. It is worth pointing out the main similarities and differences in the PL spectra for the two tungsten-based MLs. For the WS₂ spectrum, only second-order processes were required since the absolute energies are larger as compared to WSe₂ [40]. Moreover, the phonon modes exhibit larger splittings (see Supplementary Information, Table S1). The LA-TA splitting at the K point of WS₂, for example, exceeds the value in WSe₂ by ~ 4 meV. More significantly, the optical phonon energies differ by ~ 15 meV and up to ~ 20 meV at the Γ and K points, respectively.

Among the similar PL signatures is the weak peak below D and the intense peak between X and D with fine structure due to the specific optical phonon spectrum of WS₂. Akin to WSe₂, the former and the latter are assigned to acoustic and optical replicas of momentum-dark states K'₁ and K'_u, respectively. Surprisingly, best fit suggests an exchange splitting of $\Delta(K'_u - X) = 11.4$ meV in contrast to 2.7 meV for WSe₂ in Fig. 3a. The fit to WS₂ PL requires a significant upshift of the state K'_u in order to optimally accommodate the optical phonon sidebands into the intense and complexly structured

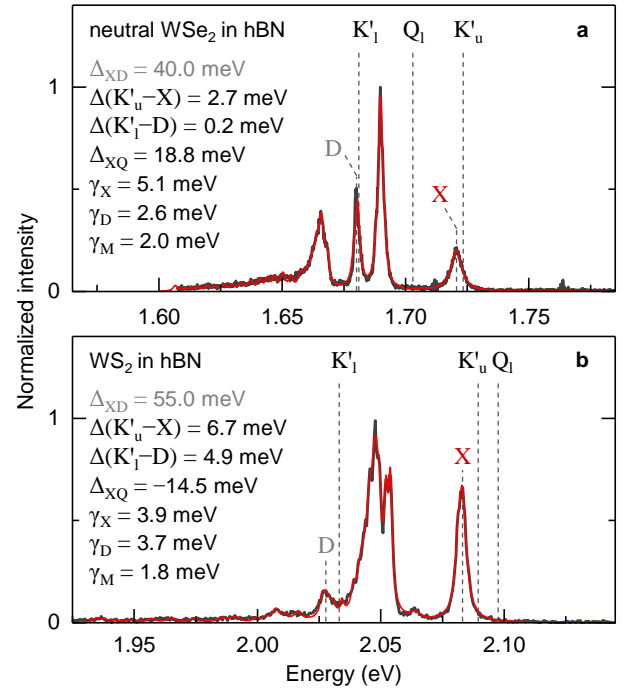


FIG. 4: **Decomposition of monolayer WSe₂ and WS₂ spectra including Q-momentum excitons.** a, b. Same as Fig. 3a, b but with involvement of Q exciton manifold placed in between the states X and D in a, and above the state X in b. Free (fixed) fit parameters are given in the legends in black (grey).

PL peak between X and D. This could be an artefact of the non-quantified contribution from trions in this sample, or indicate that the set of involved momentum-dark excitons could be expanded by the Q-exciton manifold as will be discussed in the next section.

Role of Q-momentum excitons in monolayer WSe₂ and WS₂ emission. For WSe₂ MLs the Q-momentum excitons can play an important role, since the Q-valley is in close proximity to the lowest CB minimum at K according to single-particle calculations [35, 40, 50]. Excitonic corrections have been predicted to reduce the energy level of Q-excitons well below the energy of the lowest spin-forbidden state D both in WSe₂ and WS₂ MLs [54, 55, 62]. This, however, is in contradiction to the analysis developed so far that explains the lowest-energy PL peak in terms of acoustic replicas of the momentum-dark reservoir K'₁. Any deeper momentum-dark state should exhibit large population with pronounced PL phonon sidebands as in the case of bilayer WSe₂ with momentum-indirect band gap [63]. The only two remaining scenarios for the energy position of the Q-exciton level is in between D and X or above X (apart from placing it in resonance with K'_u or K'₁ with trivial implications).

The analysis of best fits shown in Fig. 4 suggests that the first scenario is better suited to model the spectrum of ML WSe₂. Before proceeding, we note that second- and higher-order phonon-assisted processes were restricted to combina-

tions of multiple phonons with total phonon momentum of Q or K depending on the respective initial valley of the electron (see Supplementary Information for details). For example, the scattering of the electron from the Q-valley into the K-valley and subsequent emission of an optical phonon would involve an LA or TA phonon at the Q-point and a zero-momentum optical phonon at the Γ -point of the first Brillouin zone. With this approach to the best-fit, the energy position of the Q_1 state in Fig. 4a is identified at $\Delta_{XQ} \simeq 19$ meV below the bright exciton with marginal variations in other fit parameters as compared to Fig. 3a. The corresponding energy level hierarchy would assign the bright-most PL peak now to acoustic phonon replicas of the Q-exciton manifold with contributions to the lowest-energy peak via optical sidebands.

In the case of ML WS_2 in Fig. 4b, on the other hand, the second scenario performed better. It adds an explanation to the first weak PL peak below X as an acoustic sideband of Q_1 with its respective optical sidebands merging into the most intense PL peak between X and D. Moreover, this configuration reduced the conspicuously large exchange splitting between X and K'_u found in the fit of Fig. 3b, and is at least qualitatively in line with theoretical calculations that predict a small separation between Q- and K-excitons in WS_2 rather than in WSe_2 MLs [62].

Overall, within the suggested approach we find good qualitative and satisfactory quantitative description of the spectra. Its quantitative validity is limited by the assumption of identical linewidths for all momentum-dark excitons which is not necessarily the case since different phonon-assisted pathways determine the effective lifetimes of momentum-dark excitons. Moreover, as opposed to the inclusion of both in-plane and out-of-plane optical phonon modes, we discarded the out-of-plane acoustic phonon mode ZA. The experimental precision limited by the spectral broadening even in best samples [30, 39, 44] currently provides an upper bound of a few meV on these effects.

Even with the current uncertainty in the values of exchange interaction and the energetic splittings between the valleys, our model highlights the importance of the role played by momentum-dark excitons in elementary optical response of ML TMDs. The conclusions are fully in line with the interpretation of cryogenic spectra from bilayer WSe_2 [63] and $MoSe_2$ - WSe_2 heterobilayers [64]. Based on our findings, further experimental work and more precise theoretical calculations of the single-particle band structure and phonon modes will finally consolidate a quantitative understanding of excitons in TMD MLs. Placed into a broader perspective of prevalent puzzles in TMD spectroscopy [65], our analysis provides sufficient guidelines for new interpretations.

Acknowledgments: We thank G. Cassabois for fruitful discussions and P. Altpeter and R. Rath for assistance in the clean-room. This work was funded by the Volkswagen Foundation, the European Research Council (ERC) under the ERC grant agreement no. 336749, and the Deutsche Forschungsgemeinschaft (DFG) via the Cluster of Excellence Nanosystems Initiative Munich (NIM). A. H. also acknowledges sup-

port from the Center for NanoScience (CeNS) and LMUinnovativ. B. U. thanks ERC grant agreement no. 306719, ITN Spin-NANO Marie Skłodowska-Curie grant agreement no. 676108, C. R. thanks ANR MoS2ValleyControl, Programme Investissements d’Avenir ANR-11-IDEX-0002-02, reference ANR-10-LABX-0037-NEXT for financial support. M. M. G. acknowledges support from ILNACS CNRS-Ioffe and RFBR 17-52-16020. X. M. also acknowledges the Institut Universitaire de France. K. W. and T. T. acknowledge support from the Elemental Strategy Initiative conducted by the MEXT, Japan and JSPS KAKENHI Grant Numbers JP26248061, JP15K21722, and JP25106006.

-
- [1] A. Splendiani, L. Sun, Y. Zhang, T. Li, J. Kim, C.-Y. Chim, G. Galli, and F. Wang, *Nano Lett.* **10**, 1271 (2010).
 - [2] K. F. Mak, C. Lee, J. Hone, J. Shan, and T. F. Heinz, *Phys. Rev. Lett.* **105**, 136805 (2010).
 - [3] A. K. Geim and I. V. Grigorieva, *Nature* **499**, 419 (2013).
 - [4] K. Novoselov, A. Mishchenko, A. Carvalho, and A. H. Castro Neto, *Science* **353**, aac9439 (2016).
 - [5] K. F. Mak and J. Shan, *Nat. Photonics* **10**, 216 (2016).
 - [6] A. Chernikov, T. C. Berkelbach, H. M. Hill, A. Rigosi, Y. Li, O. B. Aslan, D. R. Reichman, M. S. Hybertsen, and T. F. Heinz, *Phys. Rev. Lett.* **113**, 076802 (2014).
 - [7] K. He, N. Kumar, L. Zhao, Z. Wang, K. F. Mak, H. Zhao, and J. Shan, *Phys. Rev. Lett.* **113**, 026803 (2014).
 - [8] Z. Ye, T. Cao, K. O’Brien, H. Zhu, X. Yin, Y. Wang, S. G. Louie, and X. Zhang, *Nature* **513**, 214 (2014).
 - [9] G. Wang, A. Chernikov, M. M. Glazov, T. F. Heinz, X. Marie, T. Amand, and B. Urbaszek, arXiv:1707.05863 (2017).
 - [10] D. Xiao, G.-B. Liu, W. Feng, X. Xu, and W. Yao, *Phys. Rev. Lett.* **108**, 196802 (2012).
 - [11] J. Kim, X. Hong, C. Jin, S.-F. Shi, C.-Y. S. Chang, M.-H. Chiu, L.-J. Li, and F. Wang, *Science* **346**, 1205 (2014).
 - [12] E. J. Sie, J. W. McCliver, Y.-H. Lee, L. Fu, J. Kong, and N. Gedik, *Nat. Mater.* **14**, 290 (2015).
 - [13] G. Wang, X. Marie, B. Liu, T. Amand, C. Robert, F. Cadiz, P. Renucci, and B. Urbaszek, *Phys. Rev. Lett.* **117**, 187401 (2016).
 - [14] Z. Ye, D. Sun, and T. F. Heinz, *Nat. Phys.* **13**, 26 (2017).
 - [15] E. J. Sie, C. H. Lui, Y.-H. Lee, L. Fu, J. Kong, and N. Gedik, *Science* **355**, 1066 (2017).
 - [16] T. Cao, G. Wang, W. Han, H. Ye, C. Zhu, J. Shi, Q. Niu, P. Tan, E. Wang, B. Liu, et al., *Nat. Commun.* **3**, 887 (2012).
 - [17] K. F. Mak, K. He, J. Shan, and T. F. Heinz, *Nat. Nanotechnol.* **7**, 494 (2012).
 - [18] H. Zeng, J. Dai, W. Yao, D. Xiao, and X. Cui, *Nat. Nanotechnol.* **7**, 490 (2012).
 - [19] A. M. Jones, H. Yu, N. J. Ghimire, S. Wu, G. Aivazian, J. S. Ross, B. Zhao, J. Yan, D. G. Mandrus, D. Xiao, et al., *Nat. Nanotechnol.* **8**, 634 (2013).
 - [20] W. Yao, D. Xiao, and Q. Niu, *Phys. Rev. B* **77**, 235406 (2008).
 - [21] X. Xu, W. Yao, D. Xiao, and T. F. Heinz, *Nat. Phys.* **10**, 343 (2014).
 - [22] A. Neumann, J. Lindlau, L. Colombier, M. Nutz, S. Najmaei, J. Lou, A. D. Mohite, H. Yamaguchi, and A. Högele, *Nat. Nanotechnol.* **12**, 329 (2017).
 - [23] X.-X. Zhang, Y. You, S. Y. F. Zhao, and T. F. Heinz, *Phys. Rev. Lett.* **115**, 257403 (2015).

- [24] G. Wang, C. Robert, A. Suslu, B. Chen, S. Yang, S. Alamdari, I. C. Gerber, T. Amand, X. Marie, S. Tongay, et al., *Nat. Commun.* **6**, 10110 (2015).
- [25] F. Withers, O. Del Pozo-Zamudio, S. Schwarz, S. Dufferwiel, P. M. Walker, T. Godde, A. P. Rooney, A. Gholinia, C. R. Woods, P. Blake, et al., *Nano Lett.* **15**, 8223 (2015).
- [26] M. R. Molas, C. Faugeras, A. O. Slobodeniuk, K. Nogajewski, M. Bartos, D. M. Basko, and M. Potemski, *2D Mater.* **4**, 021003 (2017).
- [27] X.-X. Zhang, T. Cao, Z. Lu, Y.-C. Lin, F. Zhang, Y. Wang, Z. Li, J. C. Hone, J. A. Robinson, D. Smirnov, et al., *Nat. Nanotechnol.* **12**, 883 (2017).
- [28] Y. Zhou, G. Scuri, D. S. Wild, A. A. High, A. Dibos, L. A. Jauregui, C. Shu, K. d. Greve, K. Pistunova, A. Joe, et al., *Nat. Nanotechnol.* **12**, 856 (2017).
- [29] Z. Wang, L. Zhao, K. F. Mak, and J. Shan, *Nano Lett.* **17**, 740 (2017).
- [30] G. Wang, C. Robert, M. M. Glazov, F. Cadiz, E. Courtade, T. Amand, D. Lagarde, T. Taniguchi, K. Watanabe, B. Urbaszek, et al., *Phys. Rev. Lett.* **119**, 047401 (2017).
- [31] G.-B. Liu, W.-Y. Shan, Y. Yao, W. Yao, and D. Xiao, *Phys. Rev. B* **88**, 085433 (2013).
- [32] K. Kořmider and J. Fernández-Rossier, *Phys. Rev. B* **87**, 075451 (2013).
- [33] K. Kořmider, J. W. González, and J. Fernández-Rossier, *Phys. Rev. B* **88**, 245436 (2013).
- [34] A. Kormányos, V. Zólyomi, N. D. Drummond, and G. Burkard, *Phys. Rev. X* **4**, 011034 (2014).
- [35] A. Kormányos, G. Burkard, M. Gmitra, J. Fabian, V. Zólyomi, N. D. Drummond, and V. Fal'ko, *2D Mater.* **2**, 022001 (2015).
- [36] K. F. Mak, K. He, C. Lee, G. H. Lee, J. Hone, T. F. Heinz, and J. Shan, *Nat. Mater.* **12**, 207 (2013).
- [37] J. S. Ross, S. Wu, H. Yu, N. J. Ghimire, A. M. Jones, G. Aivazian, J. Yan, D. G. Mandrus, D. Xiao, W. Yao, et al., *Nat. Commun.* **4**, 1474 (2013).
- [38] M. Sidler, P. Back, O. Cotlet, A. Srivastava, T. Fink, M. Kroner, E. Demler, and A. Imamoglu, *Nat. Phys.* **13**, 255 (2017).
- [39] F. Cadiz, E. Courtade, C. Robert, G. Wang, Y. Shen, H. Cai, T. Taniguchi, K. Watanabe, H. Carrere, D. Lagarde, et al., *Phys. Rev. X* **7**, 021026 (2017).
- [40] Z. Jin, X. Li, J. T. Mullen, and K. W. Kim, *Phys. Rev. B* **90**, 045422 (2014).
- [41] H. Dery and Y. Song, *Phys. Rev. B* **92**, 125431 (2015).
- [42] A. M. Jones, H. Yu, J. R. Schaibley, J. Yan, D. G. Mandrus, T. Taniguchi, K. Watanabe, H. Dery, W. Yao, and X. Xu, *Nat. Phys.* **12** (2015).
- [43] C. R. Dean, A. F. Young, I. Meric, C. Lee, L. Wang, S. Sorgenfrei, K. Watanabe, T. Taniguchi, P. Kim, K. Shepard, et al., *Nature nanotechnology* **5**, 722 (2010).
- [44] O. Ajayi, J. Ardelean, G. Shepard, J. Wang, A. Antony, T. Taniguchi, K. Watanabe, T. Heinz, S. Strauf, X.-Y. Zhu, et al., *2D Mater.* **4**, 031011 (2017).
- [45] C. Jin, J. Kim, J. Suh, Z. Shi, B. Chen, X. Fan, M. Kam, K. Watanabe, T. Taniguchi, S. Tongay, et al., *Nature Physics* (2016).
- [46] Y. Zhang, T.-R. Chang, B. Zhou, Y.-T. Cui, H. Yan, Z. Liu, F. Schmitt, J. Lee, R. Moore, Y. Chen, et al., *Nat. Nanotechnol.* **9**, 111 (2014).
- [47] G. Wang, L. Bouet, D. Lagarde, M. Vidal, A. Balocchi, T. Amand, X. Marie, and B. Urbaszek, *Phys. Rev. B* **90**, 075413 (2014).
- [48] W. Zhao, R. M. Ribeiro, M. Toh, A. Carvalho, C. Kloc, A. H. Castro Neto, and G. Eda, *Nano Lett.* **13**, 5627 (2013).
- [49] H. Liu, J. Chen, H. Yu, F. Yang, L. Jiao, G.-B. Liu, W. Ho, C. Gao, J. Jia, W. Yao, et al., *Nat. Commun.* **6**, 8180 (2015).
- [50] C. Zhang, Y. Chen, A. Johnson, M.-Y. Li, L.-J. Li, P. C. Mende, R. M. Feenstra, and C.-K. Shih, *Nano Lett.* **15**, 6494 (2015).
- [51] H. Dery and Y. Song, *Phys. Rev. B* **92**, 125431 (2015).
- [52] D. Y. Qiu, T. Cao, and S. G. Louie, *Phys. Rev. Lett.* **115**, 176801 (2015).
- [53] J. P. Echeverry, B. Urbaszek, T. Amand, X. Marie, and I. C. Gerber, *Phys. Rev. B* **93**, 121107 (2016).
- [54] M. Selig, G. Berghäuser, A. Raja, P. Nagler, C. Schüller, T. F. Heinz, T. Korn, A. Chernikov, E. Malic, and A. Knorr, *Nat. Commun.* **7**, 13279 (2016).
- [55] M. Selig, G. Berghäuser, M. Richter, R. Bratschitsch, A. Knorr, and E. Malic, arXiv:1703.03317 (2017).
- [56] D. Y. Qiu, F. H. da Jornada, and S. G. Louie, *Phys. Rev. Lett.* **111**, 216805 (2013).
- [57] J. R. Chelikowsky and M. L. Cohen, *Phys. Rev. B* **14**, 556 (1976).
- [58] G. Cassaboïs, P. Valvin, and B. Gil, *Nat. Photonics* **10**, 262 (2016).
- [59] A. Chernikov, A. M. van der Zande, H. M. Hill, A. F. Rigosi, A. Velauthapillai, J. Hone, and T. F. Heinz, *Phys. Rev. Lett.* **115**, 126802 (2015).
- [60] G. Cassaboïs, P. Valvin, and B. Gil, *Phys. Rev. B* **93**, 035207 (2016).
- [61] E. Courtade, M. Semina, M. Manca, M. M. Glazov, C. Robert, F. Cadiz, G. Wang, T. Taniguchi, K. Watanabe, M. Pierre, et al., *Phys. Rev. B* **96**, 085302 (2017).
- [62] E. Malic, M. Selig, M. Feieraben, S. Brem, D. Christiansen, F. Wendler, A. Knorr, and G. Berghäuser, arXiv:1709.00941 (2017).
- [63] J. Lindlau, M. Selig, A. Neumann, L. Colombier, J. Kim, G. Berghäuser, F. Wang, E. Malic, and A. Högele, arXiv:1710.00989 (2017).
- [64] M. Förg, L. Colombier, R. Patel, J. Lindlau, A. D. Mohite, H. Yamaguchi, D. Hunger, and A. Högele, arXiv:1710.00990 (2017).
- [65] M. Koperski, M. R. Molas, A. Arora, K. Nogajewski, A. O. Slobodeniuk, C. Faugeras, and M. Potemski, *Nanophotonics* **6**, 1289 (2017).
- [66] T. Taniguchi and K. Watanabe, *Journal of Crystal Growth* **303**, 525 (2007).
- [67] A. Castellanos-Gomez, M. Buscema, R. Molenaar, V. Singh, L. Janssen, H. S. J. van der Zant, and G. A. Steele, *2D Materials* **1**, 011002 (2014).
- [68] X. Zhang, X.-F. Qiao, W. Shi, J.-B. Wu, D.-S. Jiang, and P.-H. Tan, *Chem. Soc. Rev.* **44**, 2757 (2015).
- [69] A. Branny, G. Wang, S. Kumar, C. Robert, B. Lassagne, X. Marie, B. D. Gerardot, and B. Urbaszek, *Appl. Phys. Lett.* **108**, 142101 (2016).

SUPPLEMENTARY INFORMATION

Experimental setup

Cryogenic confocal PL spectroscopy studies were performed at 3.1 K in a closed-cycle cryostat (attocube systems, attoDRY1000) or a helium dewar at 4.2 K. The samples were positioned with piezo-steppers and scanners (attocube systems, ANP101 series and ANSxy100/Ir) into the diffraction limited spot of a low-temperature apochromatic objective with a numerical aperture of 0.82 (attocube systems, LT-APO/VISIR/0.82) and a spot size of $0.6 \mu\text{m}$. A He-Ne laser at 632 nm, a continuous wave green laser at 532 nm or a super-continuum laser (NKT Photonics, SuperK EXW-12) operated at 532 nm with a spectral width of 6 nm were used to excite the PL. A monochromator (PI, Acton SP-2558) equipped with a nitrogen-cooled silicon CCD (PI, Spec-10:100BR/LN) was used to detect PL with a spectral resolution of 0.4 meV.

Gated samples

We have fabricated van der Waals heterostructures by mechanical exfoliation from commercially available bulk crystals and very high quality hBN crystals [66]. A first layer of hBN was mechanically exfoliated and transferred onto a SiO_2 (90 nm)/Si substrate using PDMS stamping [67]. The deposition of the subsequent ML and the second hBN capping layer was obtained by repeating this procedure to complete the full stack. We also transferred a thin graphite flake between the top surface of the ML and a Au pre-patterned electrode. Carrier concentration was varied by applying a bias between this electrode and the p -doped Si substrate (back gate).

Photoluminescence and differential reflectivity

The charge doping level of ML MoSe_2 and WSe_2 was controlled with field-effect devices described above and monitored with differential reflectivity (DR). The PL and reflectivity spectra of ML MoSe_2 at the charge neutrality point are shown in Fig. S1a and b, respectively as in [61]. The reflectivity spectrum shows no signature of trion absorption. The respective PL and DR spectra of ML WSe_2 at the charge neutrality point are shown in Fig. S2a and b, respectively. As for ML MoSe_2 , the DR spectrum shows no signature of trion absorption.

We also applied our analysis to ML MoSe_2 encapsulated in hBN without active doping control. As in Fig. 2 of the main text, the PL spectrum in Fig. S3 features two bright PL peaks. In addition, the PL exhibits an extended red wing with some structure commonly ascribed to localized excitons in potentials of unintentional disorder. Here, we assume that the intensive PL peak ~ 30 meV below X is not related to trions but is instead composed of optical phonon sidebands of the

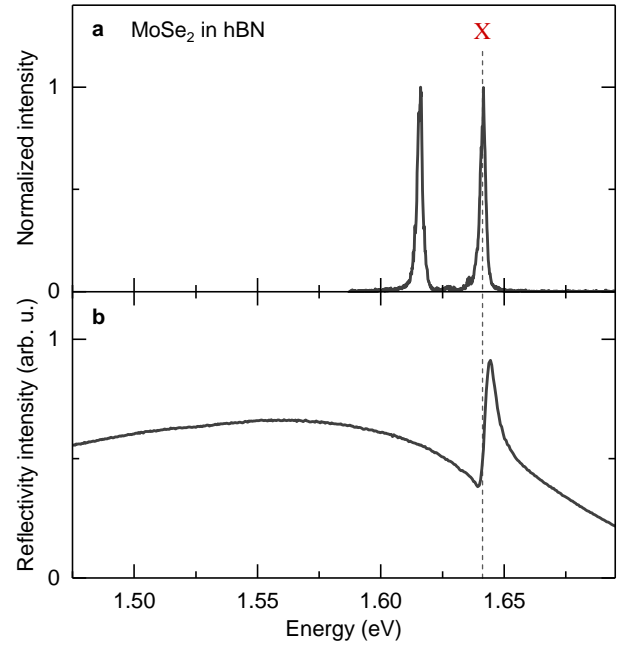


Figure S1: **a**, Photoluminescence spectrum of monolayer MoSe_2 adopted from Fig. 2 of the main text. **b**, Corresponding reflectivity at $V_g = +10$ V. Note the absence of trion-related features.

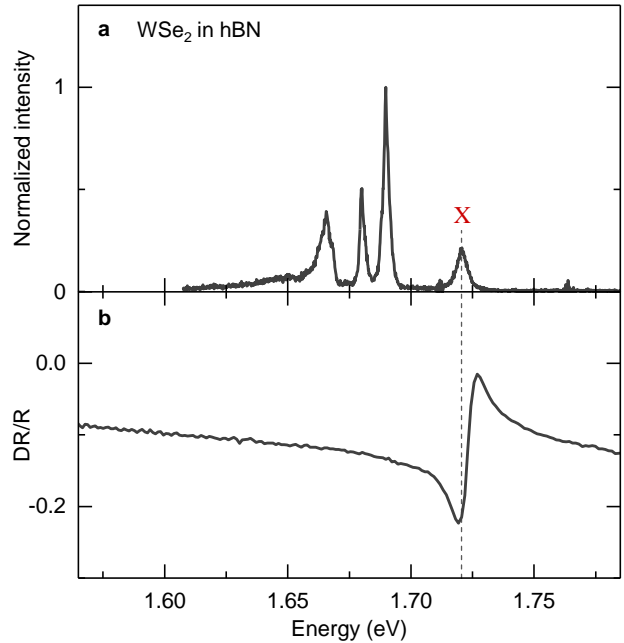


Figure S2: **a**, Photoluminescence spectrum of monolayer WSe_2 adopted from Fig. 3a of the main text. **b**, Corresponding differential reflectivity. Note the absence of trion-related features.

momentum-dark exciton state K'_u resonant with the bright exciton in the absence of electron-hole exchange.

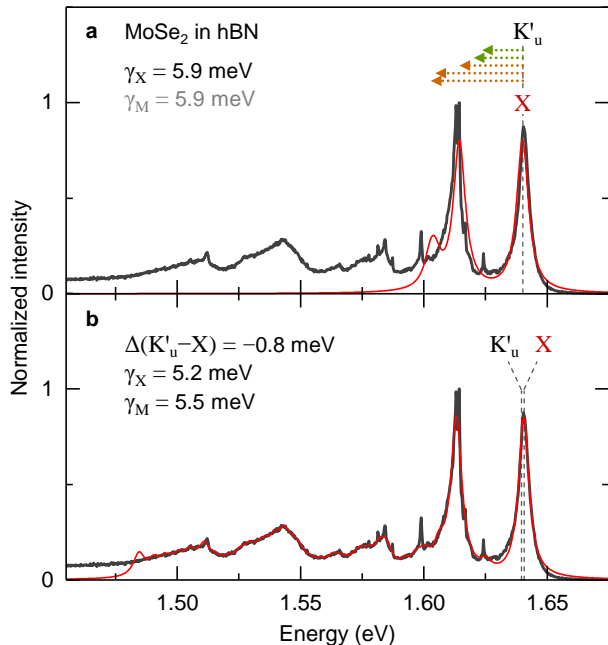


Figure S3: Spectral decomposition of cryogenic photoluminescence from monolayer MoSe₂ without active control of charge doping. **a**, Basic model fit (red solid line) with first-order phonon replicas of momentum-dark K'_u excitons resonant with the bright exciton state X in the absence of electron-hole exchange. The best-fit energy position indicated by the dashed line was obtained with γ_X as fit parameter and γ_M set identical to γ_X . The green and orange arrows indicate phonon sidebands of momentum-dark excitons associated with acoustic and optical phonons with respective energies taken from Ref. [40]. **b**, Refined model fit (red solid line) with variable energy positions and linewidths of X and K'_u states and up to fourth order phonon replicas with variable phonon energies bound by ± 2 meV around the values of Ref. [40]. Free (fixed) fit parameters are given in the legends in black (grey).

The model fit to the ML MoSe₂ spectrum of Fig. S3a was obtained with ZPLs of momentum-bright and momentum-dark excitons modeled by homogeneously broadened Lorentzians at the same energy and with the same full-width at half-maximum linewidth γ_X . Analogous to Fig. 2 of the main text, first-order scattering processes by acoustic and optical phonons with energies from Ref. 40 yield the two peaks as the main PL features with $\gamma_X = 5.9$ meV and best-fit energy positions indicated by the dashed lines.

To improve the fit up to the striking correspondence with the spectrum in Fig. S3b, we allowed the phonon energies to vary by ± 2 meV around their theoretical values. Such small variation of phonon energies account for sample-to-sample variations in the dielectric environment or strain and are well within the range of quantitative observations with Raman spectroscopy [68]. Moreover, we included phonon processes of up to fourth order (the cut-off to the model spectrum around 1.48 eV is because processes beyond fourth order were truncated), and allowed the energy positions and the

linewidths to vary for both X and K'_u states. Remarkably, all intricate features of the PL spectrum are well reproduced by the model fit without significant changes to the ZPL energies and linewidths, and with higher-order phonon processes improving the correspondence between the fit and the intricate spectral details of the extended red tail of the PL spectrum. The bright peak below X is interpreted as composed of optical phonon sidebands of the momentum-dark state K'_u that also gives rise to broad lower-energy PL peaks via its higher-order phonon replicas. In contrast, the emission from disorder-localized excitons [69], characterized by narrow spectral features in Fig. S3b, is not captured by the present model.

Mode	MoSe ₂			WS ₂			WSe ₂		
	Γ	K	Q	Γ	K	Q	Γ	K	Q
TA	0	16.6	13.3	0	17.4	15.9	0	15.6	11.6
LA	0	19.9	16.9	0	23.6	19.5	0	18.0	14.3
TO(E')	36.1	35.5	36.4	44.4	43.8	45.3	30.5	26.7	27.3
LO(E')	36.6	37.4	37.5	44.2	43.2	42.3	30.8	31.5	32.5
A ₁	30.3	25.6	27.1	51.8	48.0	50.0	30.8	31.0	30.4

TABLE S1: Phonon mode energies at the high-symmetry points of the first Brillouin zone for monolayer MoSe₂, WS₂, and WSe₂ used in the model fits. Higher order scattering processes with phonon energies equal to the energy of LO(E') within 1 meV (listed in the table in grey) were discarded from our analysis for simplicity. All energies are given in meV and reproduced from Ref. 40.

Group theory analysis

The symmetry of the Q-point is C_s with only two symmetry operations: identity and horizontal plane reflection. There are two irreducible (vector) representations of this group, namely A' (invariant) and A'' (z-coordinate, i.e. normal to the reflection plane). The intersection of the two symmetry groups C_s (Q-point) and C_{3h} (K-point) is C_s . The conduction band both at the Q- and K-points corresponds to the A' representation and, hence, transitions are possible via phonons with the same symmetry A' (these modes are symmetric under $z \rightarrow -z$). All phonon modes in question indeed correspond to this representation: acoustic E' at the Γ -point corresponds to A' at the Q-point, optical E' at the Γ -point corresponds to A' at the Q-point, and optical A'_1 at the Γ -point corresponds to A' at the Q-point. Combinations of these phonons are also allowed (provided that momentum conservation is fulfilled). With account for spin-orbit interaction all other phonons (asymmetric for $z \rightarrow -z$) are also active in K to Q transitions. In order to account for spin-orbit effects we need to also consider the spinor representations Γ_3 (spin-up, \uparrow) and Γ_4 (spin-down, \downarrow): $\Gamma_3 = A' \times \uparrow = A'' \times \downarrow$, $\Gamma_4 = A'' \times \uparrow = A' \times \downarrow$. Thus, spin-up and spin-down states can be mixed with Bloch functions of different orbital symmetry and odd in $z \rightarrow -z$ phonon modes can enable spin-flip transfer between K and Q valleys.

Transitions between the K- and K' -points can be consid-

ered analogously. To that end, we note that both elements of the wavevector group C_{3h} leave the K and K' valleys intact. The orbital Bloch functions of the conduction bands belong to the $E'(1)$ ($\sim x + iy$) and $E'(2)$ ($\sim x - iy$) irreducible representations of the C_{3h} point group. The transitions between the conduction band states are enabled by phonon modes with E' symmetry. In contrast, the orbital Bloch functions of the valence band transform according to the A' (invariant) irreducible representation. Thus, hole intervalley scattering is provided by the fully symmetric A' modes.

In the following we briefly address the activation of the spin-unlike K'_u excitons. In accordance with the symmetry analysis these states form basis irreducible representations

$E''(1)$ and $E''(2)$ of the C_{3h} point symmetry group transforming as $(x \pm iy)z$. Formally, these states can be transferred to the optically active ones by phonons with A'' symmetry (transforming like z) or by E'' phonons. Moreover, the interaction with E' phonons converts these excitons into z -polarized states. If the mirror symmetry is distorted, the $z \rightarrow -z$ operation (together with S_3 mirror rotation) should be excluded from the C_{3h} point symmetry group and the representations E'' (odd in $z \rightarrow -z$) and E' (even at $z \rightarrow -z$) cannot be formally distinguished. Hence, in experiments involving different dielectric environments at the top and the bottom of TMD MLs, A' and E'' phonons may enable activation of spin-unlike K'_u excitons.